ChemElectroChem

Research Article
doi.org/10.1002/celc.202300617

Chemistry Europe
European Chemical Societies Publishing

www.chemelectrochem.org

Gadolinium Doped Ceria as Nickel–Free Fuel Electrode in High Temperature CO_2-Electrolysis

Jan Uecker,[a, b] Ifeanyichukwu D. Unachukwu,[a, b] Vaibhav Vibhu,*[a] Izaak C. Vinke,[a] L. G. J. (Bert) de Haart,[a] and Rüdiger-A. Eichel[a, b]

In this work, the performance, electrochemical processes, and stability of GDC ($Ce_{0.8}Gd_{0.2}O_{1.9}$) fuel electrode containing single cells (GDC/8YSZ/GDC/LSCF) were examined in CO_2 electrolysis conditions. The current density and area specific resistance is determined for different operation conditions. The examined cells showed a higher performance compared to state-of-the-art Ni–YSZ fuel electrode (Ni-YSZ/8YSZ/GDC/LSCF) based single cells with a similar production route. Furthermore, the cells were examined by means of electrochemical impedance spectroscopy (EIS) and the recorded data were evaluated by the distribution of relaxation times (DRT) analysis. An equivalent circuit model (ECM) consisting of four time constants and a Gerischer impedance (LR–RQ_1–RQ_2–G–RQ_4–RQ_5) was established to gain further insight into the individual processes in the cells. For instance, the low–frequency process P_5 referring to RQ_5 is the rate-determining step in CO_2 electrolysis and is assigned to a surface reaction including the charge transfer and possibly the gas diffusion in the GDC fuel electrode. A long–term stability test was performed in CO_2 electrolysis conditions at 900 °C with a constant current load of $-0.5\ A \cdot cm^{-2}$ for up to 1200 h. A degradation rate of $62\ mV \cdot kh^{-1}$ was observed. By EIS analysis, a similar contribution of the ohmic and polarization resistances to the degradation was determined. The low–frequency process P_5 and thus the surface reaction including the charge transfer in the GDC fuel electrode is contributing most to the increase in polarization resistance. After the long–term stability test, scanning electron microscopy (SEM) analysis was carried out and a coarsening of GDC particles in the fuel electrode was observed.

Introduction

Climate change and related global warming are two of the most present challenges that are discussed in politics and society nowadays. Global warming must be kept as low as possible to minimize climate–related risks for the natural, animal, and human systems. The release of greenhouse gases including carbon dioxide (CO_2) needs to be mitigated. One CO_2 emission source is the worldwide chemical industry sector. This sector would still emit several hundred million metric megatons of CO_2 per year even in the scenario of 100% renewably generated energy use.[1] Due to the increasing demand for petrochemical products, the chemical sector is expected to grow in the upcoming years. Hence, the need for a circular carbon economy is inevitable. In industrial applications, carbon monoxide is used as a bulk chemical, for example, for the preparation of acetic acid by catalytic carbonylation of methanol or as a building block in polymers such as polyurethanes and polycarbonates.[2,3] In addition, CO can be used as a component of synthesis gas as a reaction intermediate for a variety of chemical products.[1,4–6] The sustainable conversion of CO_2 directly into CO is a solution for direct carbon capture and utilization, enabling a circular carbon economy and power-to-x scenarios.[3,7]

The use of green technologies for the electrochemical reduction of CO_2 to CO by CO_2 electrolysis is an interesting solution for the above–mentioned issues. The high temperature solid oxide electrolysis cell (SOEC) is promising due to its high faradaic efficiency and overall energy efficiency of over 75%.[3] An electrical power consumption value of ~3.4 $kWh \cdot Nm^3$ CO is reported at the SOEC stack level under CO_2 electrolysis conditions.[8] The SOEC seems to be one of the most promising technologies for the direct electrochemical reduction of CO_2 to CO.[9,10] However, for the commercialization of SOECs on a large scale, their overall stability in long–term operation needs to be improved. A significant contribution to degradation mechanisms in SOECs is caused by the fuel electrode.[11–13] The state-of-the-art fuel electrode material is Ni (nickel)-YSZ (yttria–stabilized–zirconia) cermet often combined with 8YSZ (8 mol.% yttria–stabilized zirconia) as electrolyte and LSCF ($La_{0.58}Sr_{0.4}Co_{0.2}Fe_{0.8}O_{3-\delta}$) or LSC ($La_xSr_yCoO_{3-\delta}$) as oxygen electrode. Considering the Ni–YSZ electrodes, significant degradation during operation is reported due to Ni migration, depletion, and agglomeration.[13–15] In carbon–containing fuel gases, carbon deposition could occur at the fuel electrode, which reduces the cell performance and long–term stability. In state-of-the-art

[a] J. Uecker, I. D. Unachukwu, Dr. V. Vibhu, Dr. I. C. Vinke, Dr. L. G. J. de Haart, Prof. R.-A. Eichel
Institute of Energy and Climate Research, Fundamental Electrochemistry (IEK-9), Forschungszentrum Jülich GmbH, 52425 Jülich, Germany
E-mail: v.vibhu@fz-juelich.de

[b] J. Uecker, I. D. Unachukwu, Prof. R.-A. Eichel
Institute of Physical Chemistry, RWTH Aachen University, 52074 Aachen, Germany

Supporting information for this article is available on the WWW under https://doi.org/10.1002/celc.202300617

Ni–YSZ fuel electrode–supported cells under CO_2 electrolysis conditions the observed carbon deposition severely reduces the possible operating window for commercialization.[16] Furthermore, the deposition of carbon on the Ni catalyst surface can lead to corrosion of the Ni, structural damage to the electrode and the loss of the electrode's electronic conductivity.[17,18] In literature, the development of efficient and carbon tolerant fuel electrodes, replacing Ni–YSZ, is investigated to enable more effective usage of carbon–containing fuels.[19,20] Promising candidates include ceria ($CeO_{2-\delta}$)-based materials. It is frequently reported that the incorporation of ceria into the fuel electrode efficiently reduces carbon deposition.[21,22] Even the capability of self-de-coking (self–removal of carbon deposits) of a Ni catalyst on ceria is reported by several authors.[21,23–25] Thus, the complete replacement of YSZ by gadolinium doped ceria (GDC) is discussed in literature due to the reduced carbon formation in CO_2 electrolysis conditions and the catalytic properties of GDC.[26,27] The investigation of the Ni/GDC system by Raman mapping showed that carbon deposition may be suppressed by GDC particles.[28] Ni–GDC fuel electrodes exhibit a higher electrochemical performance compared to Ni–YSZ fuel electrodes under CO_2 electrolysis conditions and are therefore the preferred choice.[26,29,30] However, Ni-containing catalysts could still catalyze the CO disproportionation via the Boudouard reaction under SOEC conditions, even in the case of Ni–GDC fuel electrodes.[11,31,32] Other degradation mechanisms such as morphology changes of the electrode structure and poisoning of the active sides will still lower the cell's performance during long–term operation in CO_2 electrolysis conditions.[30,33] For example, similar to Ni/YSZ electrodes Ni agglomeration and Ni depletion away from the electrode/electrolyte interface after long term operation of over 1000 h in Ni–GDC fuel electrodes was reported recently.[30] Therefore, the complete absence of nickel in the fuel electrode could lead to a further improvement in the stability of SOECs in CO_2 electrolysis. Asingle phase GDC fuel electrode is a promising candidate for usage in CO_2 electrolysis and might improve the cells stability.[34] A pure GDC fuel electrode is feasible due to its mixed ionic and electronic conductivity in a reducing atmosphere and at high operating temperatures. At low partial pressure of oxygen, doped ceria exhibits a valence change of Ce^{4+} to Ce^{3+} that leads to increased ionic conductivity and electronic *n*-type conductivity.[35,36] At 700 °C and an oxygen partial pressure of 10^{-23} bar, an ionic conductivity of 0.028 $S \cdot cm^{-1}$ and an electronic conductivity of 0.47 $S \cdot cm^{-1}$ are reported for GDC ($Ce_{0.8}Gd_{0.2}O_{2-\delta}$).[37] Even at low partial pressure of oxygen around 10^{-15} bar for CO_2 electrolysis conditions lower electronic conductivities values and thus higher ohmic resistances in comparison to Ni-cermets can be mitigated by employing thin electrode layers.[34,38–40] Furthermore, ceria itself is known to participate in the elementary steps of CO_2 electro–reduction and is frequently used in CO_2 conversion catalysts.[12,41] Interestingly, the ratio between Ce^{3+}/Ce^{4+} could change by applying a bias during operation in CO_2 electrolysis as indicated in literature affecting the catalytic activity and electronic conductivity of the GDC.[39,42,43]

The overall reaction of CO_2 on ceria surfaces in SOEC can be divided into three steps including; 1) the transport of charge carriers from the bulk to the surface, 2) the adsorption of CO_2 and 3) the oxygen ion incorporation, CO formation and desorption from the ceria surface.[11] However, there are no detailed studies in literature on pure single phase GDC fuel electrode single cells and their use in high temperature CO_2 electrolysis to the author's best knowledge.

In this article, the high temperature CO_2 electrolysis of solid oxide electrolyte–supported single cells (GDC/8YSZ/GDC/LSCF) with pure GDC ($Ce_{0.8}Gd_{0.2}O_{2-\delta}$) as fuel electrode material is examined. The electrochemical activity of the cells is investigated by current–voltage (IV) characteristics and electrochemical impedance spectroscopy (EIS) at a variety of operating parameters. For example, the fuel gas composition of CO_2 and CO at the fuel electrode, the gas flow rates, and the operating temperature were varied. A long–term degradation test was performed for 1200 hours at a current density of -0.5 $A \cdot cm^{-2}$, and the degradation processes were investigated by EIS analysis. Finally, post–test characterization by scanning electron microscopy with energy dispersive X-ray analysis (SEM-EDS) was carried out for a better understanding of the degradation behaviour.

Experimental Section

Single cell preparation and fabrication

Firstly, screen printing pastes of the used materials were prepared by combining the respective powders with α-terpineol and ethyl cellulose.[44] The GDC fuel electrode and GDC barrier layer were made from commercial GDC ($Ce_{0.8}Gd_{0.2}O_{1.9}$) powder supplied by the company CerProTech. The LSCF ($La_{0.58}Sr_{0.4}Co_{0.2}Fe_{0.8}O_{3-\delta}$) oxygen electrode powder was synthesized by a modified Pecheni method.[45] The resulting screen printing slurry was mixed in a planetary vacuum mixer (THINKY Mixer ARV-310) and homogenized by roll–milling.[44] For the fabrication of the electrolyte–supported single cells, 8YSZ (8 mol.% yttria–stabilized zirconia) electrolyte supports (thickness ~300 μm, diameter = 20 mm) from the company Karafol were used. In the first step, a thin GDC barrier layer (4–5 μm) was screen printed (M2-H, EKRA screen printing Technologies) on the electrolyte support and sintered at 1350 °C for 1 h under an air atmosphere. The round GDC fuel electrode was subsequently printed (ø = 12 mm, thickness ≈ 15 μm) on the other side and sintered at 1200 °C for 1 h under an air atmosphere. The chosen sintering temperature showed the highest electrochemical performance and lowest polarization resistance (R_p) value in comparison to sintering temperatures of 1250, 1300, and 1350 °C (Figure S1, supporting information). In the next step, the LSCF oxygen electrode layer (~40 μm) was applied onto the GDC barrier layer and sintered at 1080 °C for 3 h under an air atmosphere. Finally, a thin gold layer (~4–5 μm) as a current collecting layer was printed on top of the GDC fuel electrode and sintered at 900 °C for 2 h under an air atmosphere. The complete production scheme can be found in Figure S2 in the supporting information. The active area of the single cells is 0.785 cm^2. Here it is important to note that the authors assume that gold is not significantly active in the electrochemical reaction. As relatively thin fuel electrodes are used, the ohmic losses for current collection in electrodes with reduced thickness can be compensated for by contacting layers additionally to the current collector mesh.[46,47]

Electrochemical measurements

The single cells were mounted into a full ceramic measurement housing and a gold ring was used to separate the oxygen and fuel electrode sides. A detailed description of the mounting procedure can be found in the literature.[48] Pt and Au current collector meshes were used for contacting oxygen and fuel electrode, respectively. After mounting, the single cells were heated up from room temperature to 900 °C with a heating rate of 1.5 °C·min^{-1}. A gas composition of 6 nl·h^{-1} N_2 at the fuel electrode and 6 nl·h^{-1} compressed air at the oxygen electrode was used during the heat-up. After reaching 900 °C, the gas composition at the fuel electrode was directly switched to CO_2 electrolysis conditions i.e. 80 % CO_2 + 20 % CO, keeping the same flow rate of 9 nl·h^{-1} at both electrodes. The gas flow was controlled by mass flow controllers (MFC, Bronkhorst Nord®, Kamen, Germany). The electrochemical measurements were then conducted using an IVIUM VERTEX potentiostat/galvanostat (Ivium Technologies BV, Eindhoven, Netherland) with an integrated frequency response analyzer module. A NorECs Probostat (Norwegian Electro Cermacis®, NORECS, Oslo, Norway) setup was used for the electrochemical characterization of the single cells. The current–voltage characteristics (IV curves) were measured in a voltage range from 0.6 to 1.5 V with a scanning rate of 10 mV·s^{-1}. Impedance data were recorded under potentiostatic control with 50 mV ac amplitude in a frequency range from 0.1 to 100 kHz with 12 data points per frequency decade. The electrochemical measurements were carried out under various operating conditions including various operating temperatures, different gas flow rates, and changing gas compositions at the fuel and oxygen electrodes. In the last step, a long–term stability test was performed with 80 % CO_2 + 20 % CO (9 nl·h^{-1}) gas composition at 900 °C and a constant load of −0.5 A·cm^{-2}.

Microstructural analysis

The electrode microstructure of the single cells before and after the long–term test was investigated with a Quanta FEG 650 (FEI©) scanning electron microscope equipped with an EDS detector at 20 kV. For this purpose, the single cells were embedded in epoxy resin and then well–polished along the cross–section. Lastly, a Cu tape was wrapped around the samples and a thin Au layer was sputtered on top to avoid charging effects. Quantitative analysis for the evaluation of grain sizes was done using the software ImageJ. The separation of the grains is done by watershed segmentation.[49] The grain size is obtained by following the procedure described in literature.[50]

Results and Discussion

Electrochemical Performance

To investigate the performance and feasibility of the GDC fuel electrode containing single cells in high temperature CO_2-electrolysis conditions, dc current–voltage measurements were performed at different operation conditions. The obtained IV curves at various operating temperatures, flow rates, CO_2 contents at the fuel electrode, and O_2 contents at the oxygen electrode, are shown in Figure 1a–d, respectively. For each operating condition, the open circuit voltage (OCV) was in good agreement with the theoretical ones derived by the Nernst equation. The experimental OCVs and corresponding theoretical values are presented in Table TS1–TS4 in the supporting information. From the figures, it can be noted that all IV curves exhibit a smooth transition between SOEC and SOFC mode. In the case of the charge transfer as rate–limiting step this indicates a reversible charge transfer for the investigated operating conditions. Therefore, GDC fuel electrode seem to be a feasible choice for reversible SOCs.[51] Moreover, reducing the operating temperature leads to a clear decrease in current density over the whole voltage range (Figure 1a). The trend can be explained by for example lower kinetic activities and less electronic conductivity in the GDC fuel electrode at lower temperatures.[35] The variation of IV curves with fuel gas flow rates is shown in Figure 1b, and it can be observed that a lower flow rate of 1 nl·h^{-1} leads to a very small decrease in current density of 0.02 mA·cm^{-1} compared to 9 nl·h^{-1} at 1.5 V. Therefore, a variation in flow rate in this operation window is not significantly influencing the performance of the GDC single cells. Conversely, a significant change in cell performance is observed by changing the CO_2 content (Figure 1c). The cell performance is decreased by decreasing the CO_2 content. In general, the reduction of CO_2 content reduces the available reactant and can lead to mass transport limitations, which occur mainly at high operating current densities.[3] A steepening of the slope in the IV curves (Figure 1c) at 1.4 V could indicate those mass transport limitations taking place for a gas composition of 50 % CO_2 + 50 % CO at 900 °C. However, as discussed before the flow rate and thus the reduction of the total amount of CO_2 had no significant influence on the cell performance. Therefore, another explanation is the increase in OCV caused by lowering the CO_2 content and increasing the CO content which results in a bigger total voltage difference between OCV and 1.5 V. A decrease in O_2 content at the oxygen electrode does not influence the cell performance in SOEC mode as shown in Figure 1d. Though, in SOFC mode the performance visibly decreases with lower O_2 content.

A maximum current density of 0.79 A·cm^{-2} is observed in CO_2-electrolysis at 1.5 V and 900 °C with 80 % CO_2 + 20 % CO fuel gas mixture. In an earlier study, our work group investigated the performance of Ni–GDC and Ni–YSZ fuel electrodes under CO_2 electrolysis conditions for similarly produced electrolyte–supported single cells (fuel electrode/8YSZ/GDC/LSCF).[30] The cells exhibited current densities of 1.16 A·cm^{-2} for Ni–GDC and 0.63 A·cm^{-2} for Ni–YSZ at 1.5 V and 900 °C with the same gas composition of 80 % CO_2 + 20 % CO at the fuel electrode. Thus, the single phase GDC fuel electrode exhibited higher performance than the state-of-the-art Ni-YSZ fuel electrode and around 70 % of the current density of the Ni–GDC fuel electrode in high temperature CO_2 electrolysis (Figure S3). In summary pure GDC electrodes in single cells are feasible for utilization in high temperature CO_2 electrolysis and are showing similar values compared to state-of-the-art Ni-YSZ electrodes. This supports the findings recently reported for GDC symmetrical cells.[34] However, pure GDC cells show lower performance compared to Ni–GDC cells and thus have to be modified for higher performance based on the results gathered by impedance analysis discussed later in the manuscript.

The obtained polarisation resistances (R_p) at OCV and current densities at 1.5 V ($|i|_{1.5V}$) for a variation of CO_2 content

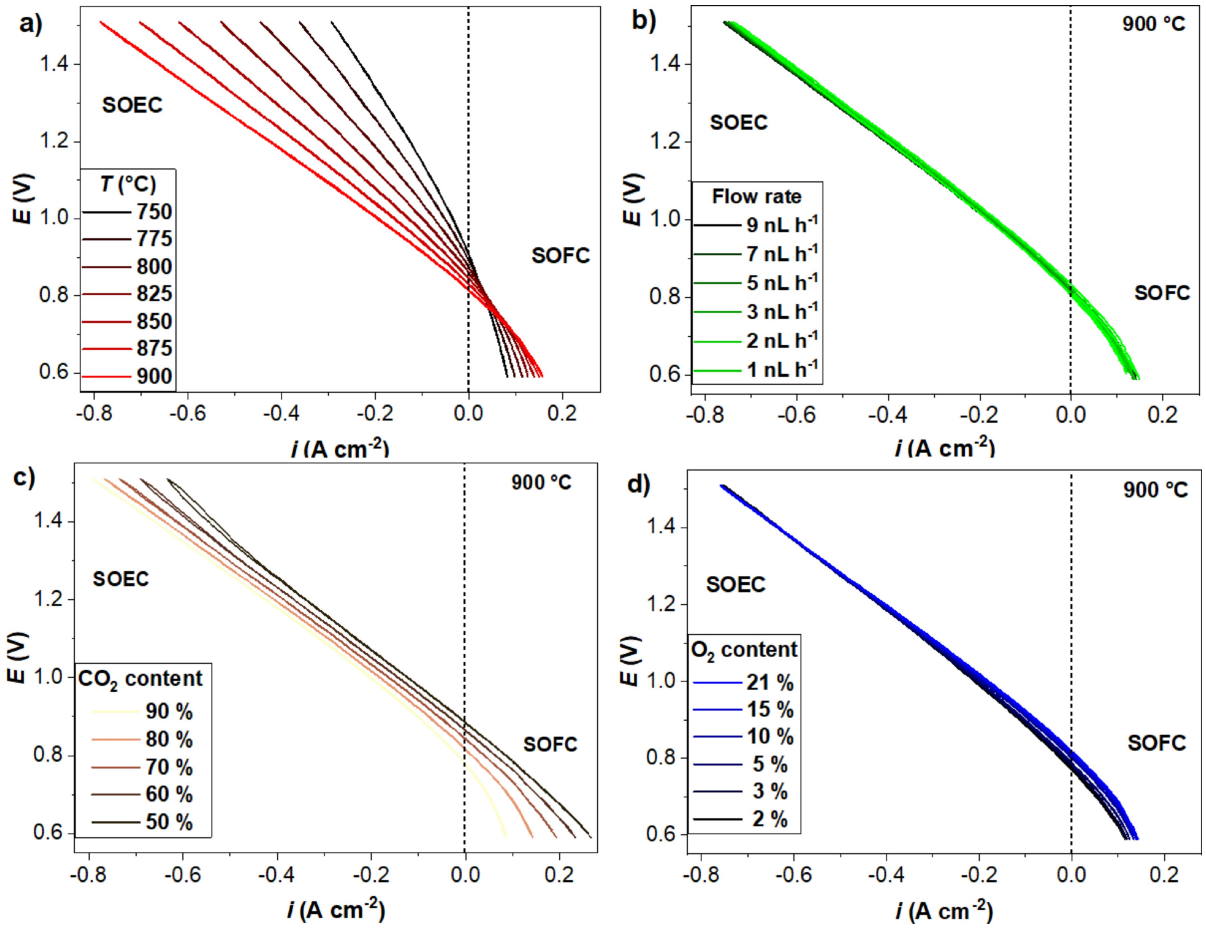

Figure 1. IV curves recorded for: (a) a variation of operating temperatures for a CO_2:CO ratio of 80:20 at 9 nl·h^{-1}; (b) a variation of flow rate for a CO_2:CO ratio of 80:20 at 900 °C; (c) a variation of CO_2:CO ratio at 9 nl·h^{-1} and 900 °C; (d) a variation of O_2 content at the oxygen electrode at 9 nl·h^{-1} and 900 °C with N_2 as balance gas.

at the fuel electrode, p_{O2} at the oxygen electrode, and the flow rate at 900 °C and 750 °C are presented in Figure 2a–c, respectively. An increase in R_p with increasing CO_2 content is observed at OCV conditions for both 900 and 750 °C (Figure 2a). The contrary trend is observed for the current density at 1.5 V which is increasing significantly from −0.63 to −0.79 A·cm^{-2} (+ ~25%) at a temperature of 900 °C from 50% CO_2 to 90% CO_2 content whereas at 750 °C a minor increase from −0.27 to −0.3 A·cm^{-2} (+~10%) is observed. The R_p is slightly increasing with a decrease in p_{O2} for both temperatures. The current density at 1.5 V is only marginally influenced by a variation in the partial pressure of oxygen at the oxygen electrode for both temperatures. Moreover, a slight decrease in R_p with an increase in flow rate for both temperatures can be observed. In accordance, the current density at 1.5 V is slightly lowered by a decrease in flow rate. The observed contrary trend between the R_p at OCV and the current density at high voltages for a variation of CO_2 content at the fuel electrode was previously reported for Ni–YSZ fuel electrode based single cells under CO_2 electrolysis.[3] The increase in R_p with increasing CO_2:CO ratio at OCV, could be explained by a higher electrochemical activity towards CO oxidation than CO_2 reduction at OCV conditions. Both reactions are governed by the carbonate as an intermediate species on ceria or doped ceria surfaces.[42,52] The driving force for the reduction of CO_2 to carbonate is higher compared to the oxidation of CO to carbonate and thus the reaction barrier for CO_2 reduction is higher compared to CO oxidation.[42,52] Furthermore, a higher activation energy of CO_2 desorption or preferential adsorption of CO_2 on the GDC surface could explain the observation.[38]

Electrochemical impedance spectroscopy analyses

Dependency on a variation of operating temperature

In the next step the GDC fuel electrode single cells are investigated by electrochemical impedance analysis to gather informations about the rate determining step during operation. This gives an outlook how to improve Ni-free ceria based fuel electrodes in future work and increase their performances. First, the variation of operating temperature from 750 °C to 900 °C at a fuel gas composition of 80% CO_2 + 20% CO is discussed. In Figure 3a, the impedance data recorded at OCV as a function of temperature are presented in a Nyquist plot. In the plots, two distinct arcs can be identified, one appearing at low relaxation

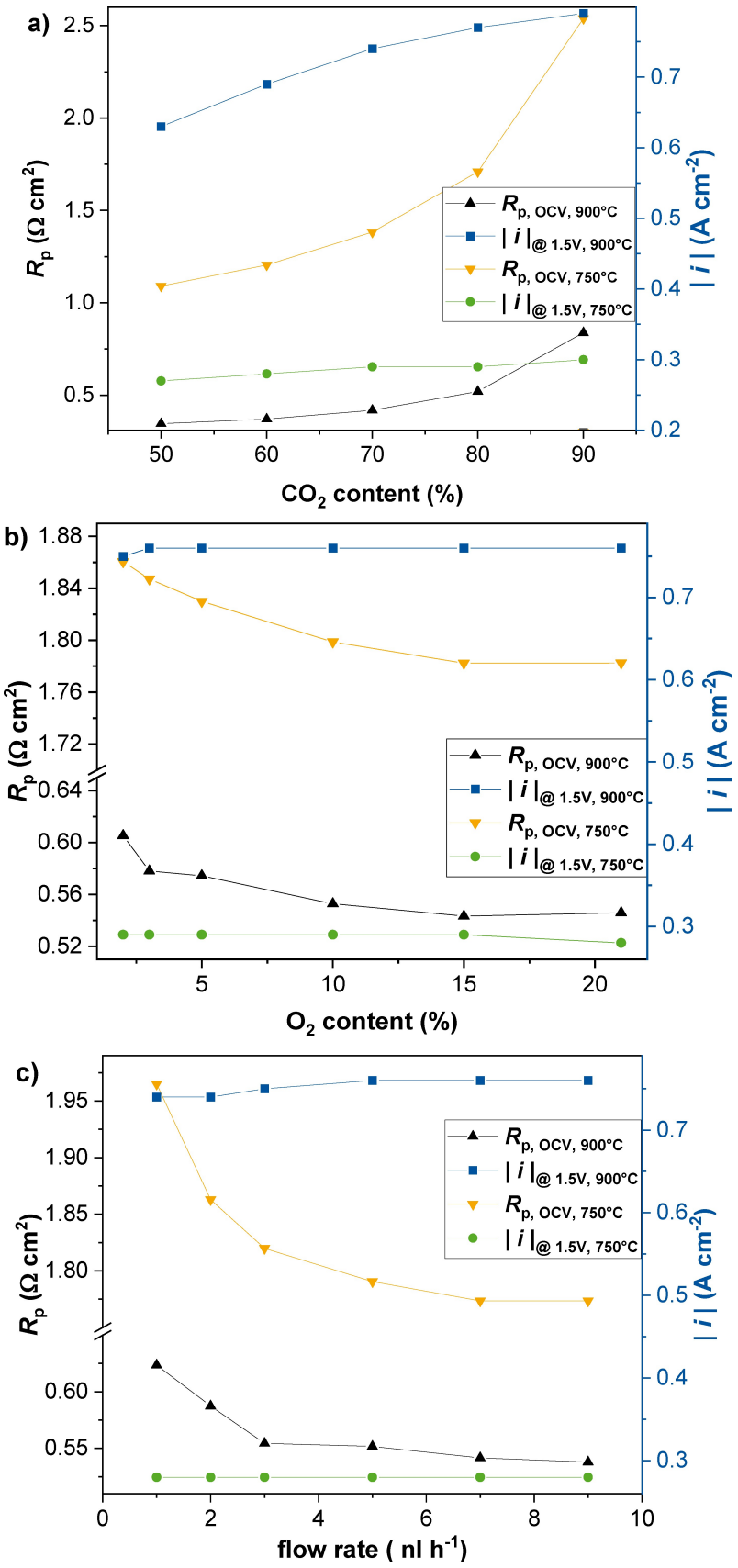

Figure 2. R_p at OCV and $|i|$ at 1.5 V at operating temperatures of 900 °C and 750 °C and their dependency with the variation of (a) CO_2 content at the fuel electrode (flow rate at both electrodes 9 nl·h^{-1}), (b) oxygen content at the oxygen electrode (flow rate at both electrodes 9 nl·h^{-1}), and (c) the flow rate at each of the electrodes.

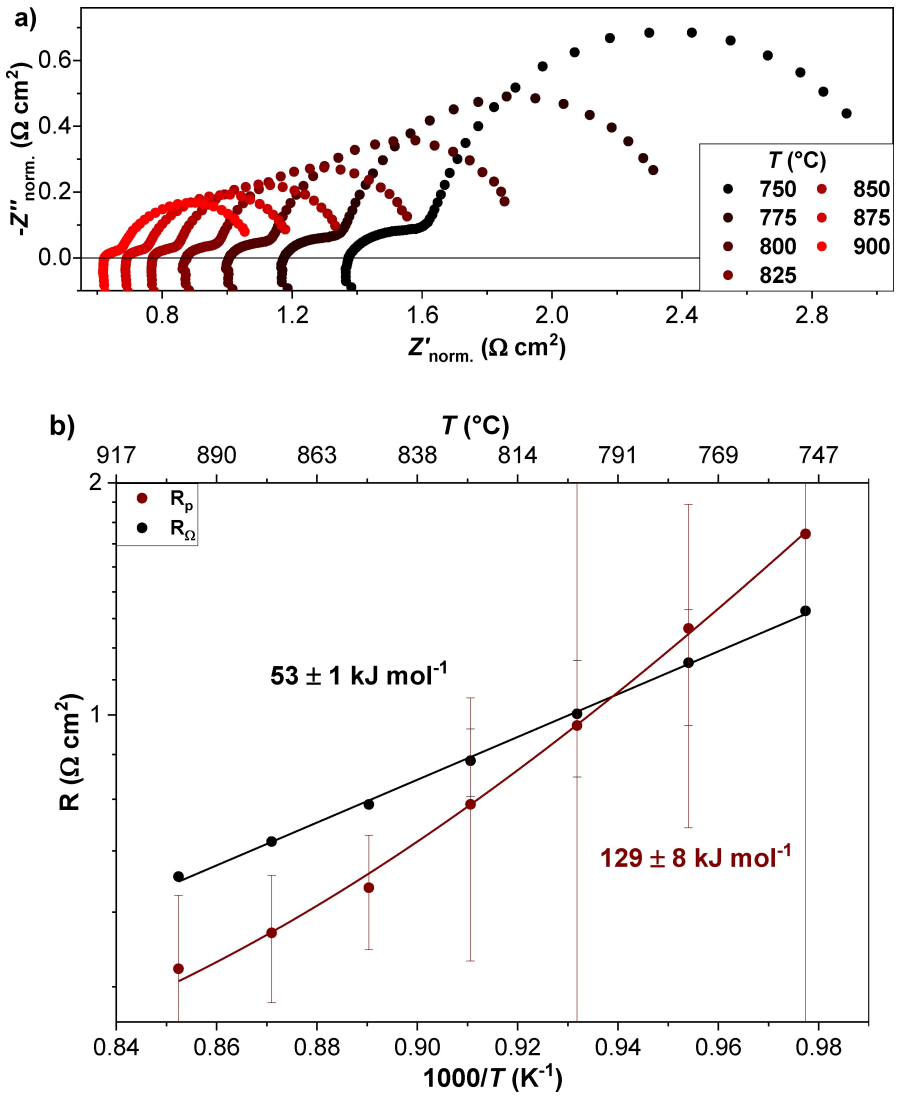

Figure 3. (a) Nyquist plots and (b) Arrhenius plot of R_Ω and R_p in a temperature range from 750 °C to 900 °C for the single cells containing a GDC fuel electrode.

frequencies and the other at higher frequencies. For all temperatures, the low frequency arc is dominating compared to the high frequency arc. Both arcs increase in magnitude with the lowering of the operating temperature and are thus thermally activated processes. Therefore, the variation of temperature is influencing the ohmic resistance (R_Ω) and R_p of the single cells. The R_Ω is obtained from the intercept with the imaginary impedance axis at high frequencies. The *R*p was derived from the evaluated EIS measurement data. The activation energies of R_Ω and R_p are calculated from the slope of the Arrhenius equation. The corresponding Arrhenius plots are shown in Figure 3b. The obtained activation energy of 52 ± 1 kJ·mol^{-1} for R_Ω is close to the values of ionic conductivity of YSZ electrolyte films in literature.[30,53] Thus, the thick electrolyte seems to be the main contribution to R_Ω. In the case of R_p it can be observed that it follows Arrhenius behaviour up to 825 °C and the slope flattens at higher temperatures. R_p seems to be increasingly governed by a low thermally activated process moving to higher temperatures. The fitting was done by considering a thermally activated contribution and a temperature independent contribution (R_{diff}) as described in literature.[34] Detailed fitting results can be found in Table S5 in the supporting information. An activation energy of 129 ± 8 kJ·mol^{-1} is observed for R_p. In literature, activation energies of around 105 kJ·mol^{-1} (1.1 eV)[34] and 100 kJ·mol^{-1}[38] are obtained for GDC fuel electrode symmetrical cells under CO_2 electrolysis conditions which are slightly lower compared to our investigated single cells. Furthermore, for Ni–GDC fuel electrode single cells, activation energies of 62 ± 1 kJ·mol^{-1}[30] and 93 kJ·mol^{-1}[54] are reported for R_p under CO_2 electrolysis conditions which is lower compared to the value obtained in our GDC single cells.

For further information about the main contribution to the higher activation energy of pure GDC fuel electrode cells, the impedance data were examined by the distribution of relaxation times (DRT) analysis. In Figure 4a, the respective DRT

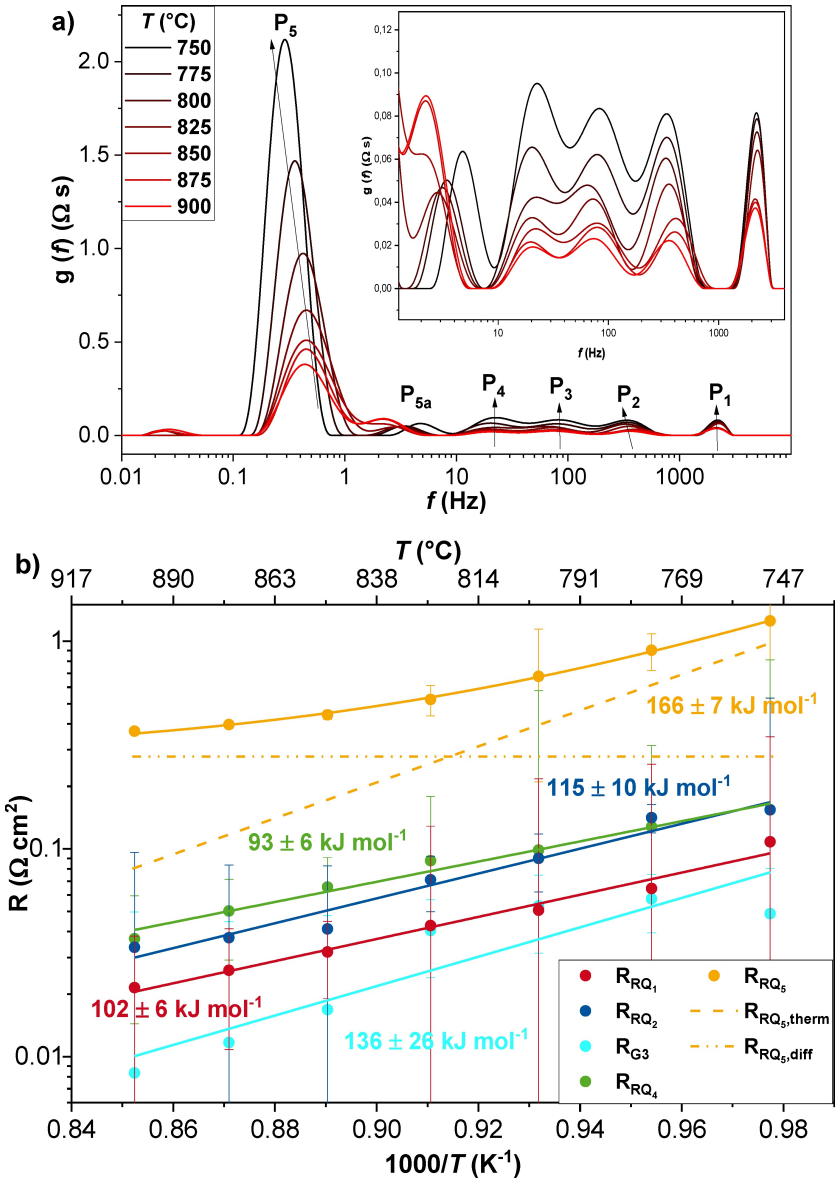

Figure 4. (a) DRT spectra of the recorded impedance data and (b) Arrhenius plots of the resistances derived by ECM fitting for CO_2 electrolysis conditions. All results are gathered from EIS measurements at OCV in the temperature range from 750 °C to 900 °C.

spectra in dependence on a variation in operating temperature are shown. In total, six peaks are observed in the DRT plots for the investigated frequency range from 0.1 Hz to 100 kHz. The peak P_5 (0.1–2 Hz) dominates the DRT spectra over the whole temperature range and thus can be referred to as a rate–limiting time constant under CO_2-electrolysis conditions. Furthermore, it shifts towards lower relaxation frequencies and increases in magnitude with a decrease in operating temperature. The peak labelled as P_{5a} is assigned as a satellite peak of the high magnitude peak P_5. The peaks P_4 (10–50 Hz), P_3 (40–200 Hz), P_2 (200–900 Hz) and P_1 (1000–3000 Hz) seem to not shift significantly with the variation of temperature. All peaks are thermally activated and increase in magnitude with a decrease in operating temperature. It can be observed, that P5 is only slightly increasing in magnitude in a temperature range from 900 °C to 850 °C. In a lower temperature domain (850 °C to 750 °C) the increase in magnitude seems to be larger. This phenomenon could explain the two temperature domains observed for R_p and will be further analyzed by equivalent circuit model (ECM) fitting.

The number of time constants gives a first estimation of the number of processes taking place during the operation of the cell. By fitting the recorded EIS data to an equivalent circuit model (ECM), the data can be further analysed. An ECM containing five time–constants with four RQ-elements in series and a Gerischer element is used where one RQ-element consists of a resistor (R) in parallel with a constant phase element (Q). An additional resistor and an inductor in series account for the ohmic resistance and the inductive contribution from the measurement system in the high frequency region, respectively. The use of other ECMs led to higher error values for the individual resistances, could not sufficiently describe the

recorded impedance data for all operation parameters, or showed different trends as the DRT analysis indicated. As seen in the error plot in Figure S4 the measured data shows good agreement with the simulation of the fit and the obtained residuals exhibited random behavior. The peaks P_1, P_2, P_3, P_4 and P_5 in the DRT correspond to the circuit elements RQ_1, RQ_2, G, RQ_4, and RQ_5, respectively. By comparing the derived activation energies (Figure 4b) with literature values first assumptions regarding the origin of the electrode process can be made.

In this work, the process P_1 exhibits a relatively high activation energy of $102 \pm 6\ kJ \cdot mol^{-1}$ and a high relaxation frequency of around 2500 Hz. P_2 shows a slightly higher activation energy of $115 \pm 10\ kJ \cdot mol^{-1}$ and an intermediate relaxation frequency of around 400 Hz. A similar value is reported in literature where an activation energy of $124 \pm 28\ kJ \cdot mol^{-1}$ was assigned to the diffusion of oxygen on the LSCF surface and through the bulk and/or pores of LSCF electrodes with an intermediate to high relaxation frequency.[55] Therefore, it could be a feasible assignment for P_1 or P_2. Furthermore, charge transfer processes and ionic transport show strong temperature dependency and high activation energies.[56–58] The process P_3 described by the Gerischer element exhibits a high activation energy of $136 \pm 26\ kJ \cdot mol^{-1}$ and a relaxation frequency between 30–200 Hz. In literature, an intermediate frequency process described by a Gerischer element is often used to describe the surface kinetics coupled with O^{2-} diffusion in the oxygen electrode bulk and an activation energy of around $140\ kJ \cdot mol^{-1}$ at a relaxation frequency of 2–500 Hz is observed.[59,60] Thus, this would fit with the observed intermediate frequency process P_3. The process P_4 exhibits an activation energy of $93 \pm 6\ kJ \cdot mol^{-1}$. Various literature studies report an activation energy of around 90–$100\ kJ \cdot mol^{-1}$ for the conduction mechanism of oxide ions in the GDC material which fits well with the values obtained for P_4.[38,61–64] The process P_5 exhibits the highest resistance values along the investigated temperatures in agreement with the DRT analysis. A flattening of the linear trend can be observed as the temperature increases like the observed trend of R_p discussed at the beginning of the chapter. This can be due to an overlap of at least two processes in the case of P_5 at a similar relaxation frequency. The lower temperature activation at higher temperatures of P_5 can be explained by an increasing relative contribution of a lower thermally activated process. Therefore, the flattening of the slope was treated as described in literature with a constant resistance contribution which is named $R_{RQ5,diff}$.[34] A high activation energy of $166 \pm 7\ kJ \cdot mol^{-1}$ is observed for the thermally activated processes ($R_{RQ5,thermal}$) in P_5. The Arrhenius behaviour of $R_{RQ5,diff}$ and $R_{RQ5,thermal}$ is displayed by the dashed lines in Figure 4b and the complete fitting results can be found in Table S5 in the supporting information. One study reported similar high activation energies for the charge transfer in the CO_2 reduction on ceria or ceria doped materials.[39] The temperature independent process can be likely assigned to a gas diffusion process by comparison with literature results on single cells.[34,59,60] A clear assignment of the processes from the activation energies is difficult in a single cell with contribution from the fuel and oxygen electrode. Thus, to further assign/separate the oxygen and fuel electrode processes, impedance analyses with the variation of gas compositions were carried out and are discussed in the next sections. Moreover, to assign the oxygen electrode processes, the impedance data of the single cell was compared with the symmetrical half–cell of LSCF.

Comparison of a single cell with a symmetrical LSCF cell

In order to separate fuel and oxygen electrode processes occurring during operation, Figure 5 shows the comparison of DRT plots of a GDC fuel electrode single cell with an LSCF symmetrical cell. A slight deviation in the relaxation frequency and magnitude of the peaks in the DRTs between the two cells is observed and can be explained by minor temperature

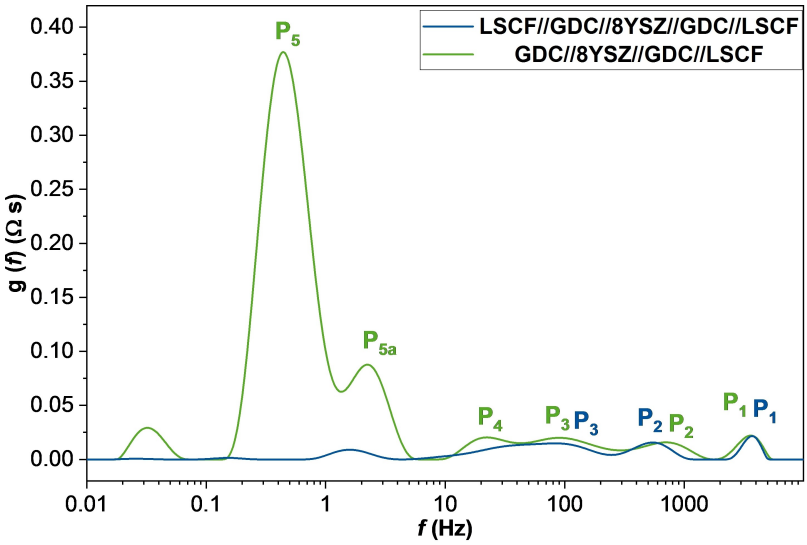

Figure 5. Comparison of a GDC fuel electrode single cell and an LSCF oxygen electrode symmetrical cell.

differences or minor leakages in the single cell measurement, which can be excluded in symmetrical cells. The processes P_1, P_2 and P_3 seem to be present in the symmetrical LSCF cells and the GDC single cells while P_4 and P_5 are rather unique for the single cells. Therefore, the results suggest an assignment of P_1, P_2 and P_3 to the oxygen electrode. Possible oxygen electrode processes that would be feasible assignments are inferred from literature sources, as the focus of this paper is on the novel GDC fuel electrode. For instance, Chen et al[65] examined the influence of fabrication methods on the performance of LSCF oxygen electrodes in symmetrical SOCs with samarium doped ceria (SDC) as electrolyte material. They assigned in their DRT analysis the high frequency peak (1000 Hz) to the charge transfer process at the LSCF/SDC interface. Furthermore, for a temperature of 700 °C, they observed peaks in their DRT in the intermediate frequency region (10–500 Hz) and assigned them to the surface exchange and ion diffusion process. Lastly, they noticed a low–frequency peak (1–10 Hz) and ascribed it to the gas diffusion in the electrode. In addition, at an intermediate frequency (2–500 Hz) an oxygen surface exchange process coupled with the oxide diffusion in the bulk of their LSCF oxygen electrode is reported.[59,66] Thus, process P_1 could be assigned the charge transfer in the LSCF oxygen electrode or at the LSCF/GDC interface due to its high activation energy, high relaxation frequency and similar literature results. The processes P_2 and P_3 could be assigned to the surface exchange in the oxygen electrode coupled with bulk and surface oxygen ion diffusion in the LSCF oxygen electrode. In the supporting information, the dependency of the resistances to a variation in oxygen content at the oxygen electrode is discussed for the single cell (Figure S5c). The results show that at least one process e.g. P_3 in the intermediate frequency range is influenced by a variation in oxygen content. Other processes do not show any clear tendency with the variation of p_{O2}. In summary, the results indicate that processes P_1, P_2 and P_3 are oxygen electrode processes and P_4 and P_5 can be assigned to the investigated pure GDC fuel electrode. This will be further confirmed in the next step by varying the fuel content at the fuel electrode.

Dependency with gas variation at the fuel electrode

For further investigations and confirmation of fuel electrode processes, impedance measurements under different CO_2:CO compositions were performed and analysed by DRT analysis and ECM fitting. In Figure 6a, the respective Nyquist plots for a variation of the CO_2:CO ratio recorded at OCV and 900 °C are shown. An increase in CO_2 led to an increase in the R_p value, whereas the ohmic resistance was not significantly influenced but moving to slightly higher resistance with an increase in CO_2 content. The low frequency arc is significantly increasing in magnitude, whereas no significant changes in the intermediate and high frequency region are visible. In Figure 6b, the respective DRT spectra in dependency on a variation in CO_2:CO ratio are shown. The high to intermediate peaks P_1, P_2 and P_3 show no significant dependency on a change in fuel gas composition. The peak P_4 shows minor fluctuations and decreases slightly in magnitude from 50% CO_2 to 60% CO_2 content at the fuel electrode. However, a clear trend cannot be observed. In contrast, the peak P_5 exhibits a pronounced dependence on a CO_2 variation, increasing in magnitude with an increase in CO_2 content. The results obtained by ECM fitting are presented in Figure 6c. The resistances R_{RQ1}, R_{RQ2}, R_{RG3} and R_{RQ4} show no visible dependency on a variation in CO_2 content at the fuel electrode. The resistance R_{RQ5} shows an increase in value which is pronounced visible at a CO_2 content between 70% and 90%. Thus, the trend observed by ECM fitting follows the results obtained by DRT analysis. The authors want to note here that the ohmic resistance is slightly increasing with an increase in CO_2 content due to an increase in the partial pressure of oxygen and lower electronic conductivity of the GDC material as shown in Figure S6 in the supporting information.[34] However, the increase is not significantly influencing the cell performance due to the relatively low GDC fuel electrode thickness.[34]

In summary, the process corresponding to the high magnitude and low frequency peak P_5 can be assigned to the fuel electrode due to its dependency on a variation in fuel gas and its nonexistence in the LSCF symmetrical cells. As discussed earlier, the resistance R_5 corresponding to process P_5 contributes the most to the R_p of the single cells and thus is the rate–determining process in the GDC fuel electrode single cells. In literature, many studies investigated the CO_2 reduction on ceria cermet surfaces and there is a consensus that a surface reaction including the transfer of two electrons to a physisorbed CO_2 molecule is the rate–determining step.[11,39,42,67] Thus, the resistance R_{RQ5} was fitted by the Butler–Volmer equation as frequently applied in SOCs.[66,68] The resistance R_{RQ5} exhibits Butler–Volmer type behaviour with a charge transfer coefficient of $\alpha_{R5,900\,°C} = 0.558$ at 900 °C and $\alpha_{R5,750\,°C} = 0.701$ at 750 °C in a potential range from 0.8 to 1.3 V in CO_2 electrolysis conditions (Figure S7). Generally, a theoretical charge transfer coefficient of 0.5 is assumed for the charge transfer at an electrode.[69] Thus, a feasible assignment of P_5 would be a surface reaction including a charge transfer at the GDC fuel electrode based on literature studies, the high activation energy and its Butler–Volmer type behaviour. However, an overlapping with a gas diffusion or gas conversion process which is normally seen at low relaxation frequencies is likely as discussed previously.[3,44] In the case of Ni–GDC fuel electrodes, it has been shown that surface reactions are shifted from a high relaxation frequency to the low frequency region due to the high chemical capacitance of the GDC which could explain the low relaxation frequency of P_5 in our cells.[60,62,70]

In the case of P_4, an assignment to the ionic diffusion in the GDC fuel electrode is feasible due to the similar activation energy in comparison with values reported for GDC in literature, the nonexistence in the LSCF symmetrical cells and the nonsignificant dependency on a change in fuel gas composition. Furthermore, a similar process (2–50 Hz) with a fairly insensitive behaviour relating to the gas composition in was observed in Ni–GDC fuel electrode symmetrical cells.[62] They assigned it to the oxide ion transport to or on the fuel electrode

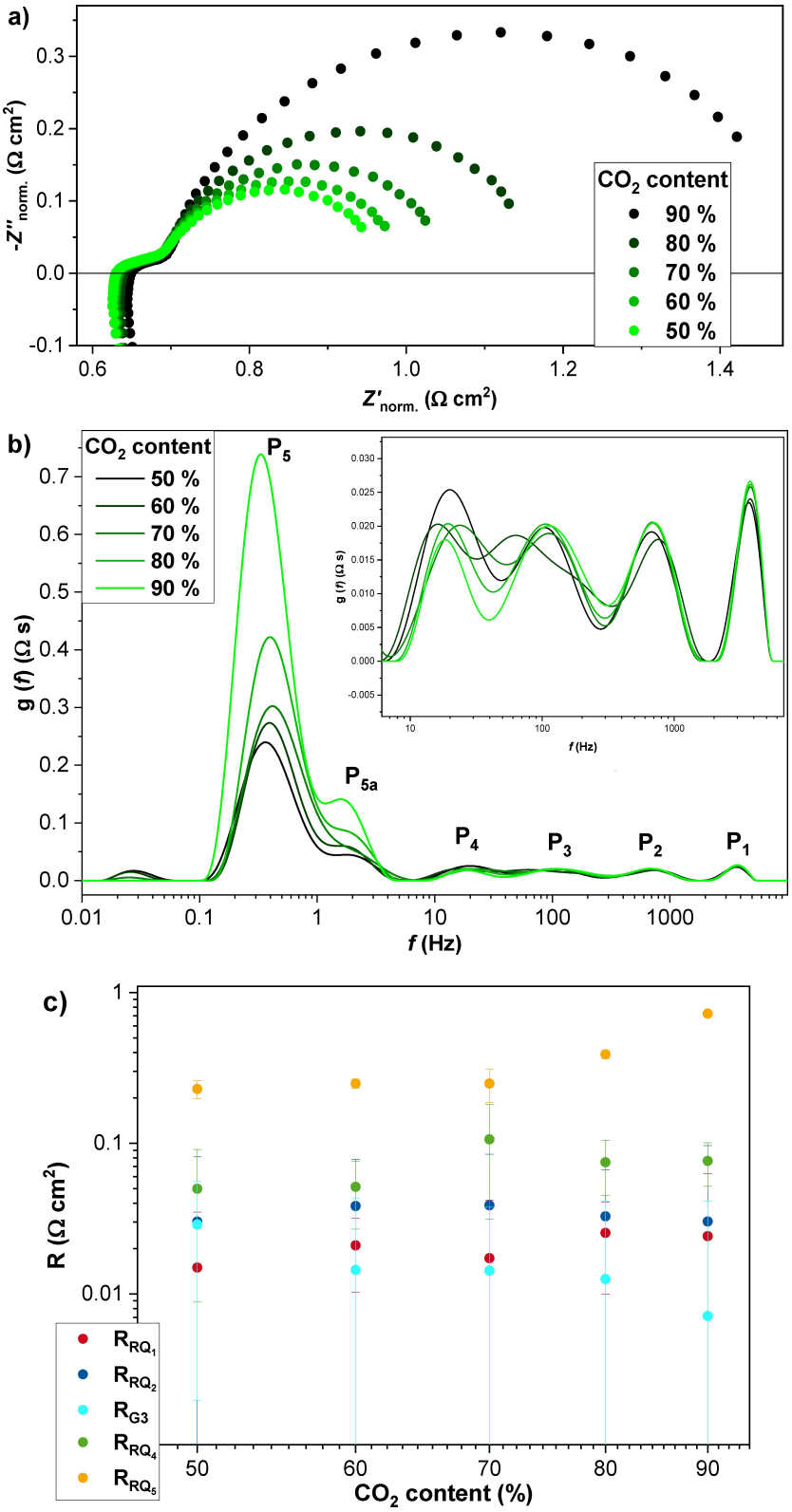

Figure 6. (a) Nyquist plots, (b) DRT spectra and (c) resistances derived by ECM fitting as a function of CO_2 content at the fuel electrode.

surface. In Table 1, a summary of a possible electrochemical process assignment related to the individual polarisation resistances for the investigated GDC/8YSZ/GDC/LSCF single cells is given. In summary, in further experiments the surface reaction including the charge transfer at the GDC electrode has to be improved for higher performance values. One possibility

Table 1. Assigned feasible electrochemical reaction processes in the GDC single cell of the fuel electrode processes.

Time constant/ Process	Frequency range	Activation energy ($kj \cdot mol^{-1}$)	Dependencies	Assignment
P_4 (R_4)	1–30 Hz	93 ± 6	Temperature, low $p_{CO2,\ fuel}$	Ionic diffusion in/at the GDC fuel electrode
P_5 (R_5)	0.1–3 Hz	166 ± 7	Temperature, $p_{CO2,\ fuel}$, low $p_{O2,\ oxygen}$	Surface reaction including a charge transfer at the GDC fuel electrode + gas diffusion

is the doping of the GDC fuel electrode with (transition–) metals or/and nanoparticles from metals (alloys) as described in literature for perovskite based Ni-free fuel electrodes.[71,72] This can lead to enhanced CO_2/CO activation processes and lower CO_2 reduction reaction energy.

Long–term stability test under CO_2 electrolysis conditions

Long–term stability test

The produced GDC/YSZ/GDC/LSCF single cells were used for a stability test up to 1200 h under CO_2 electrolysis conditions at a constant current load of $-0.5\ A \cdot cm^{-2}$ and 900 °C with 80 % CO_2 + 20 % CO gas mixture at the fuel electrode side (4.5 $nl \cdot h^{-1}$ CO_2 + 4.5 $nl \cdot h^{-1}$ CO flow at the fuel electrode side and 9 $nl \cdot h^{-1}$ compressed air at the oxygen electrode side). The recorded degradation curve of the GDC fuel electrode single cell is presented in Figure 7. The stability measurement had to be restarted two times due to power interruptions in the lab at around 900 h of degradation time which is visualized by the two arrows in Figure 7. A degradation rate of 62 $mV \cdot kh^{-1}$ was calculated over the whole degradation time including the two power interruptions. A slightly lower degradation rate of 56 $mV \cdot kh^{-1}$ is calculated for the first 900 h of the stability experiment which was conducted without interruptions in the measurement. Furthermore, after the first 500 hours of operation, a slight change in degradation rate can be observed. In the first 500 hours, a degradation rate of 53 $mV \cdot kh^{-1}$ is calculated and in the time range from 500 to 900 hours, a slightly higher rate of 60 $mV \cdot kh^{-1}$ is observed. In comparison, for similar produced Ni-GDC/8YSZ/GDC/LSCF single cells a significantly lower degradation rate of 31 $mV \cdot kh^{-1}$ at a constant load of $-0.5\ A \cdot cm^{-2}$ and a gas mixture of 80 % CO_2 + 20 % CO at 900 °C is reported.[30] However, in comparison to the state-of-the-art Ni-YZ fuel electrode containing single cell, a lower degradation rate is observed as Kim–Lohsoontorn and Bea[26] showed rapid degradation in CO_2 electrolysis conditions.

Electrochemical investigation of the degraded cell

For further insights into the degradation mechanism, IV curves and impedance measurements were taken at the start (t = 0 h) and the end (t = 1200 h) of the stability test. In Figure 8a, the respective IV characteristics are shown. A decrease in current density over the entire voltage range is observed. At 1.5 V the current density decreased from 0.76 $A \cdot cm^{-2}$ to 0.65 $A \cdot cm^{-2}$ The

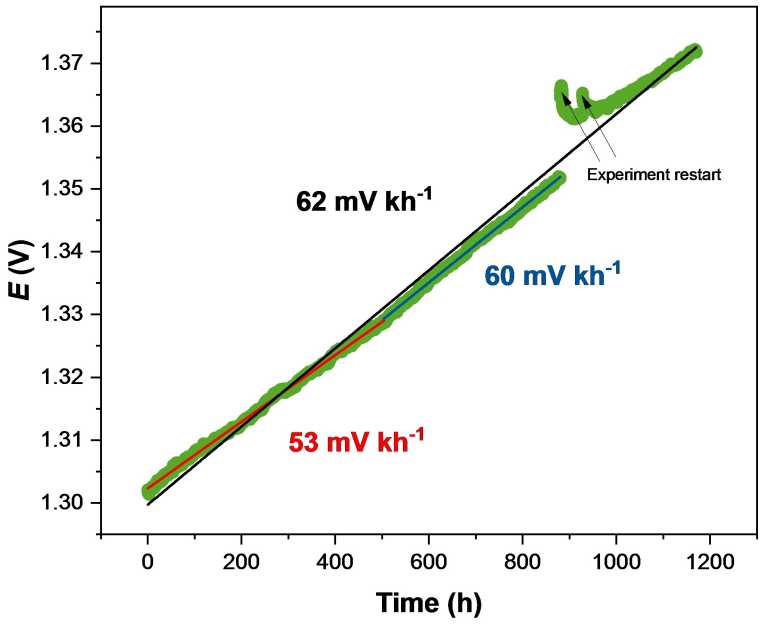

Figure 7. Long–term stability test as a variation of cell voltage as a function of degradation time.

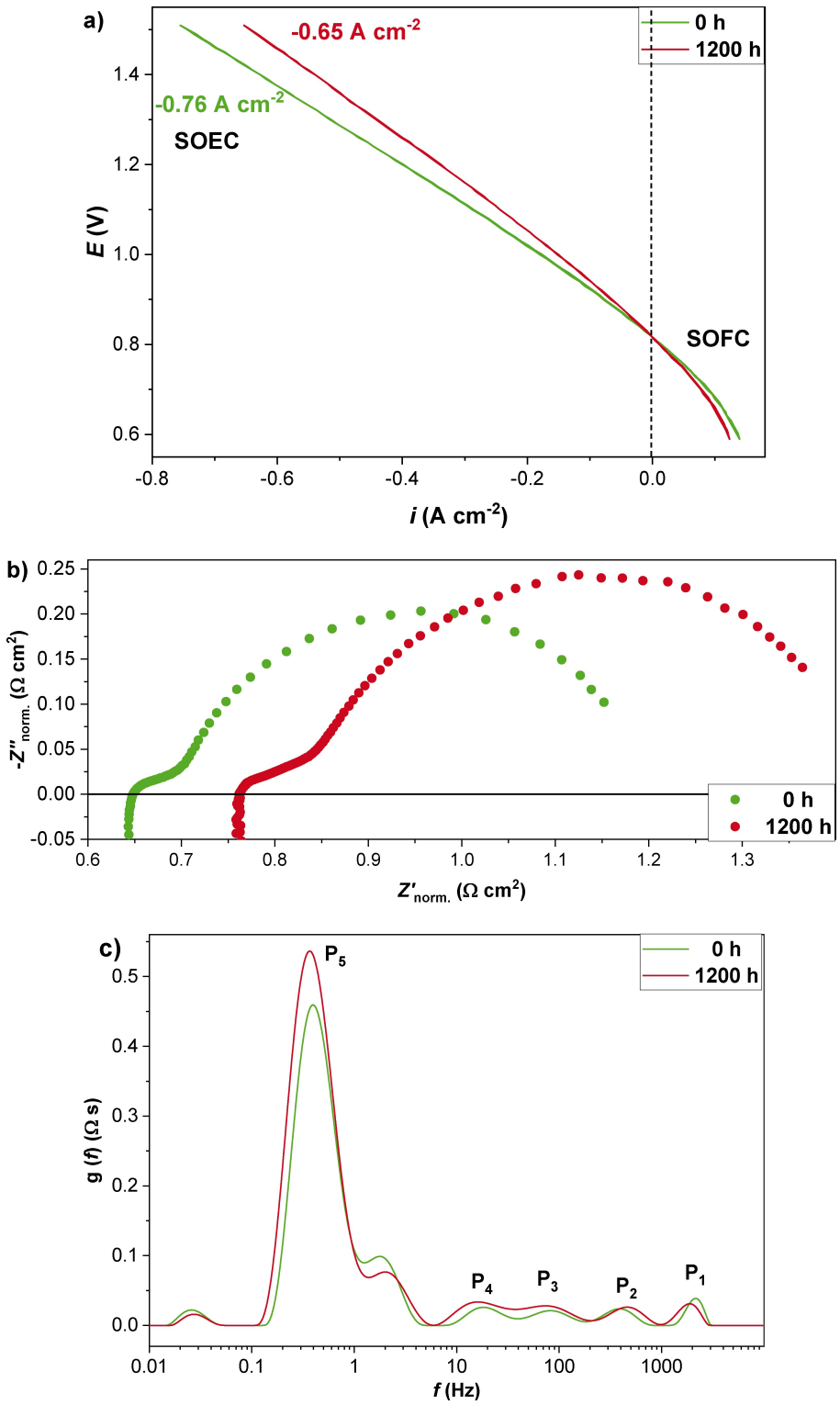

Figure 8. (a) IV curves, (b) Nyquist plots at OCV and (c) DRT spectra at the start (t = 0 h) and end (t = 1200 h) of the long–term stability test.

respective Nyquist plots recorded at OCV are shown in Figure 8b. An increase in ohmic resistance after the degradation test is visible, moving from 0.64 to 0.76 $\Omega \cdot cm^2$. Furthermore, the polarisation resistance increased by 0.12 $\Omega \cdot cm^2$ from 0.54 to 0.66 $\Omega \cdot cm^2$ at OCV. In general, the loss of electrode contact with the current collector results in an increase in the ohmic resistance and thus an increase in degradation rate. Such ohmic resistance increase due to loss of contact surface is usually accompanied by a proportional increase in the R_p, which is not observed in our case. It indicates that ohmic resistance is most

likely, not due to contact loss. The DRT plots before and after the stability test are shown in Figure 8c. After the long–term stability test, the peak P_5 is significantly increasing in magnitude. Furthermore, the peaks P_4 and P_3 show a slight increase in magnitude. The peaks P_2 and P_1 exhibit no significant change. In conclusion, the process P_5 which was assigned to a surface reaction including the charge transfer and the gas diffusion in the GDC fuel electrode is the main source of the degradation during the polarization of the single cells. The LSCF oxygen electrode does not seem to show a significant influence on the loss of performance in the long–term stability test. Interestingly, our group reported a similar influence of the GDC fuel electrode and a high contribution of the LSCF oxygen electrode to the performance loss of GDC/8YSZ/GDC/LSCF single cells in steam electrolysis conditions.[73]

Microstructural analysis of the degraded cell

After the long–term stability test up to 1200 h, the degraded single cell was embedded in an epoxy resin alongside a freshly prepared heated–up cell. The cells were mirror–polished along the cross–section before SEM-EDX analysis. There are no significant differences visible in the 8YSZ electrolyte, GDC barrier layer/8YSZ interface or GDC barrier layer/LSCF interface in the as–prepared and degraded cell, as shown in Figure 9. In addition, no significant change is observed at the GDC fuel electrode/YSZ interface before and after the stability test and the GDC fuel electrode seems still well attached to the 8YSZ electrode after the degradation test. However, coarsening of the GDC particles and thus densification of the pore structure is observed on the fuel electrode side. By analyzing five SEM images of the fuel electrode before and after the degradation by the software ImageJ utilizing the watershed method the average grain sizes can be obtained.[49,50] The fuel electrode before the degradation exhibits an average grain size of 270 ± 12 µm[73] whereas after the degradation the grain sizes increase significantly to 560 ± 30 µm. In literature, a coarsening of GDC particles was already observed by our workgroup after a long–term degradation test in steam electrolysis conditions.[73] Furthermore, the loss in GDC percolation and coverage of Ni particles by using GDC is reported in the literature in the case of Ni–GDC fuel electrodes in reducing conditions.[74,75]

The LSCF oxygen electrode and the GDC barrier show no significant changes before and after degradation. Furthermore, from the SEM pictures, no clear evidence of frequently reported degradation mechanisms such as Sr (strontium)–segregation and the formation of an insulating $SrZrO_3$ (strontium zirconium oxide) layer at the 8YSZ electrolyte can be observed.[46,76,77] Moreover, the EDX analysis (Figure S8) shows no Sr at the electrolyte interface and no formation of cobalt–oxide particles in the LSCF structure after the long–term stability test.

The results examined by SEM-EDX analysis support the results gathered by EIS data. The increase in R_p was mainly attributed to the GDC fuel electrode which can be explained by the coarsening of GDC particles in the electrode structure. The coarsening could lead to a decrease in active surface area for the reduction of CO_2 and thus lower performance.

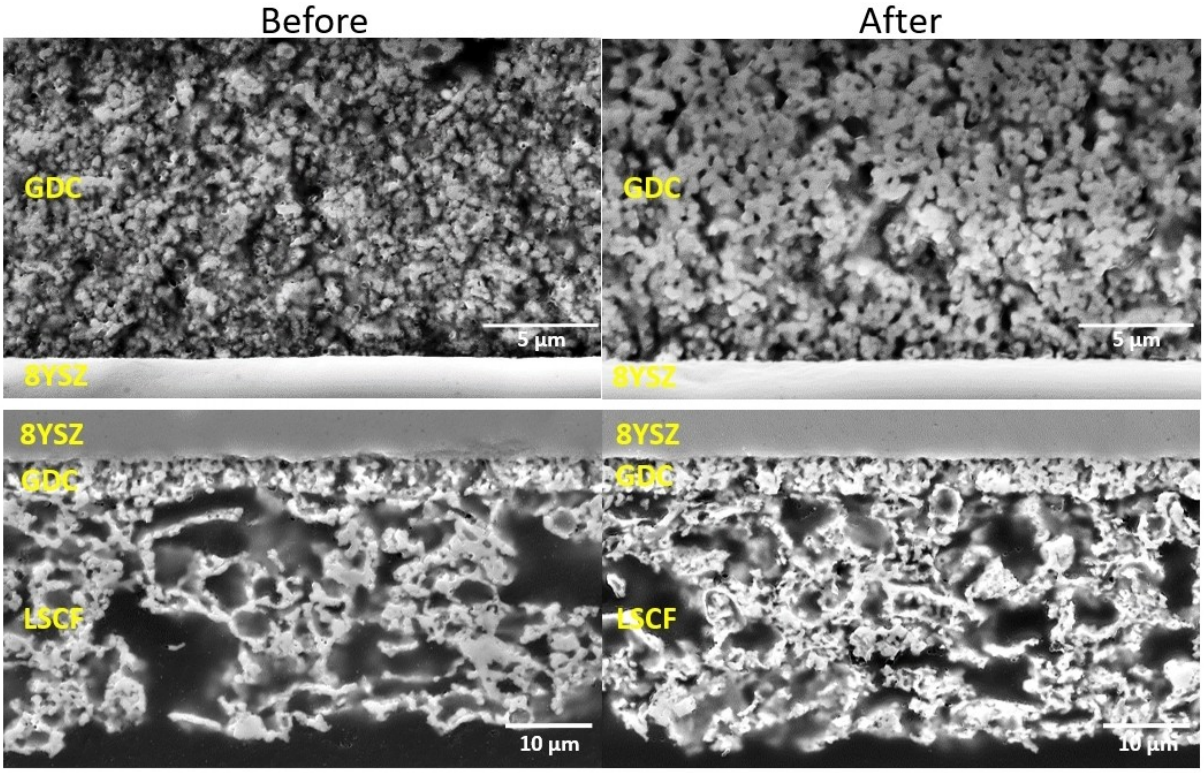

Figure 9. SEM pictures of a GDC fuel electrode single cell before and after the long-term stability test.

Conclusions

In conclusion, the GDC fuel electrode single cells showed a current density of 0.79 $A \cdot cm^{-2}$ at 1.5 V and thus a higher performance compared to the state-of-the-art Ni-YSZ fuel electrode and around 70% of a Ni–GDC fuel electrode single cell. Furthermore, five processes were distinguished with EIS, DRT and ECM analysis during operation. The low frequency process P_5 (0.1–3 Hz) and the intermediate frequency process P_4 (1–30 Hz) were assigned to the surface reaction including a charge transfer process plus gas diffusion and ionic diffusion in/at the GDC fuel electrode, respectively. In addition, it was observed that P_5 is the rate–determining process during CO_2 electrolysis as it contributes most to the R_p of the single cells. However, a contribution of a low frequency gas diffusion process to P_5 cannot be excluded. In long–term operation, a degradation rate of 62 $mV \cdot kh^{-1}$ was observed, which is larger than that of Ni–GDC fuel electrode single cells investigated under similar conditions. The degradation is attributed to an similar increase in R_Ω and R_p after 1200 h operation time. Furthermore, the EIS and SEM analysis showed that the increase in R_p could be related to a coarsening of GDC particles in the fuel electrode.

Acknowledgments

The authors gratefully acknowledge funding by the German Federal Ministry of Education and Research (BMBF) within the iNEW 2.0 Project: incubator sustainable and renewable value chains, under grant agreement number 03SF0627A. Open Access funding enabled and organized by Projekt DEAL.

Conflict of Interests

The authors declare no conflict of interest.

Data Availability Statement

The data that support the findings of this study are available on request from the corresponding author. The data are not publicly available due to privacy or ethical restrictions.

Keywords: CGO · Degradation · Electrochemical performance · GDC · Nickel–free fuel electrodes · SOECs

[1] S. R. Foit, L. Dittrich, T. Theuer, S. Morgenthaler, R.-A. Eichel, L. G. J. de Haart, *White Syngas by Co-Electrolysis for Industrial Chemistry ECS Transactions, 91* **2019**, 2467.
[2] J. Bierhals, *Carbon Monoxide* Ullmann's Encyclopedia of Industrial Chemistry, Volume 6, Wiley-VHC, 2001 .
[3] S. Foit, L. Dittrich, T. Duyster, I. Vinke, R.-A. Eichel, L. G. J. de Haart, *Direct Solid Oxide Electrolysis of Carbon Dioxide: Analysis of Performance and Processes Processes* **2020**, *8*, 1390.
[4] L. Dittrich, M. Nohl, E. E. Jaekel, S. Foit, L. G. J. de Haart, R.-A. Eichel, *High-Temperature Co-Electrolysis: A Versatile Method to Sustainably Produce Tailored Syngas Compositions* Journal of The Electrochemical Society, *166*, **2019**, F971.
[5] T. Theuer, D. Schäfer, L. Dittrich, M. Nohl, S. Foit, L. Blum, R.-A. Eichel, L. G. J. de Haart, *Sustainable Syngas Production by High-Temperature Co-electrolysis, Chemie Ingenieur Technik 92* **2020**, 40–44.
[6] S. R. Foit, I. C. Vinke, L. G. J. de Haart, R.-A. Eichel, *Power-to-Syngas: An Enabling Technology for the Transition of the Energy System? Angewandte Chemie International Edition, 56*, **2017**, 5402–5411.
[7] S. van Bavel, S. Verma, E. Negro, M. Bracht, *Integrating CO2 Electrolysis into the Gas-to-Liquids-Power-to-Liquids Process* ACS Energy Letters, **2020**, *5*, 2597–2601.
[8] R. Küngas, P. Blennow, T. Heiredal-Clausen, T. Holt Nørby, J. Rass-Hansen, J. B. Hansen, P. G. Moses, *Progress in SOEC Development Activities at Haldor Topsøe, ECS Transactions* **2019**, *91*, 215.
[9] R. Küngas, *J. Electrochem. Soc.* **2020**, *167*, 044508.
[10] A. Hauch, R. Küngas, P. Blennow, A. B. Hansen, J. B. Hansen, B. V. Mathiesen, M. B. Mogensen, *Science* **2020**, *370*, eaba6118.
[11] E. M. Sala, N. Mazzanti, M. B. Mogensen, C. Chatzichristodoulou, *Solid State Ionics* **2022**, *375*, 115833.
[12] Y. Song, X. Zhang, K. Xie, G. Wang, X. Bao, *Challenges, and Prospects, Advanced Materials* **2019**, *31*, 1902033.
[13] M. B. Mogensen, M. Chen, H. L. Frandsen, C. Graves, A. Hauch, T. Jacobsen, S. H. Jensen, T. L. Skafte, X. Sun, *ECS Trans.* **2019**, *91*, 613.
[14] M. S. Khan, S.-B. Lee, R.-H. Song, J.-W. Lee, T.-H. Lim, S.-J. Park, *Ceram. Int.* **2016**, *42*, 35–48.
[15] M. Trini, A. Hauch, S. De Angelis, X. Tong, P. V. Hendriksen, M. Chen, *J. Power Sources* **2020**, *450* 227599.
[16] T. L. Skafte, P. Blennow, J. Hjelm, C. Graves, *J. Power Sources* **2018**, *373*, 54–60.
[17] T. Chen, W. G. Wang, H. Miao, T. Li, C. Xu, *J. Power Sources* **2011**, *196*, 2461–2468.
[18] A. Singh, J. M. Hill, *J. Power Sources* **2012**, *214*, 185–194.
[19] J. C. Ruiz-Morales, J. Canales-Vázquez, C. Savaniu, D. Marrero-López, W. Zhou, J. T. S. Irvine, *Nature* **2006**, *439*, 568–571.
[20] M. D. Gross, J. M. Vohs, R. J. Gorte, *J. Mater. Chem.* **2007**, *17*, 3071–3077.
[21] C. J. Laycock, J. Z. Staniforth, R. M. Ormerod, *Dalton Trans.* **2011**, *40*, 5494–5504.
[22] J. Xu, C. M. Y. Yeung, J. Ni, F. Meunier, N. Acerbi, M. Fowles, S. C. Tsang, *Appl. Catal. A* **2008**, *345*, 119–127.
[23] T.-J. Huang, T.-C. Yu, *Catal. Lett.* **2005**, *102*, 175–181.
[24] T.-J. Huang, H.-J. Lin, T.-C. Yu, *Catal. Lett.* **2005**, *105*, 239–247.
[25] J. B. Wang, Y.-S. Wu, T.-J. Huang, *Appl. Catal. A* **2004**, *272*, 289–298.
[26] P. Kim-Lohsoontorn, J. Bae, *J. Power Sources* **2011**, *196*, 7161–7168.
[27] V. Duboviks, R. C. Maher, M. Kishimoto, L. F. Cohen, N. P. Brandon, G. J. Offer, *Phys. Chem. Chem. Phys.* **2014**, *16*, 13063–13068.
[28] M. Yoshinaga, H. Kishimoto, K. Yamaji, Y.-P. Xiong, M. E. Brito, T. Horita, H. Yokokawa, *Solid State Ionics* **2011**, *192*, 571–575.
[29] V. Singh, H. Muroyama, T. Matsui, S. Hashigami, T. Inagaki, K. Eguchi, *J. Power Sources* **2015**, *293*, 642–648.
[30] I. D. Unachukwu, V. Vibhu, I. C. Vinke, R.-A. Eichel, L. G. J. de Haart, *J. Power Sources* **2023**, *556*, 232436.
[31] S. D. Ebbesen, M. Mogensen, *J. Power Sources* **2009**, *193*, 349–358.
[32] Z. Zhan, W. Kobsiriphat, J. R. Wilson, M. Pillai, I. Kim, S. A. Barnett, *Energy Fuels* **2009**, *23*, 3089–3096.
[33] M. B. Mogensen, M. Chen, H. L. Frandsen, C. Graves, A. Hauch, P. V. Hendriksen, T. Jacobsen, S. H. Jensen, T. L. Skafte, X. Sun, *Fuel Cells* **2021**, *21*, 415–429.
[34] A. Nenning, M. Holzmann, J. Fleig, A. K. Opitz, *Materials Advances* **2021**, *2*, 5422–5431.
[35] S. Wang, T. Kobayashi, M. Dokiya, T. Hashimoto, *J. Electrochem. Soc.* **2000**, *147*, 3606.
[36] S. Lübke, H. D. Wiemhöfer, *Solid State Ionics* **1999**, *117*, 229–243.
[37] D. L. Maricle, T. E. Swarr, S. Karavolis, *Solid State Ionics* **1992**, *52*, 173–182.
[38] R. D. Green, C.-C. Liu, S. B. Adler, *Solid State Ionics* **2008**, *179*, 647–660.
[39] Z. Zhao, M. Uddi, N. Tsvetkov, B. Yildiz, A. F. Ghoniem, *Phys. Chem. Chem. Phys.* **2017**, *19*, 25774–25785.
[40] A. Shaur, M. Drazkowski, S. Zhu, B. Boukamp, H. J. M. Bouwmeester, *J. Mater. Chem. A* **2023**, *11*, 25020–25030.
[41] K. Chang, H. Zhang, M.-j. Cheng, Q. Lu, *ACS Catal.* **2020**, *10*, 613–631.
[42] Z. A. Feng, M. L. Machala, W. C. Chueh, *Phys. Chem. Chem. Phys.* **2015**, *17*, 12273–12281.
[43] Y. Yu, B. Mao, A. Geller, R. Chang, K. Gaskell, Z. Liu, B. W. Eichhorn, *Phys. Chem. Chem. Phys.* **2014**, *16*, 11633–11639.

[44] I. D. Unachukwu, V. Vibhu, J. Uecker, I. C. Vinke, R.-A. Eichel, L. G. J. de Haart, *J. CO2 Util.* **2023**, *69*, 102423.
[45] P. Courty, H. Ajot, C. Marcilly, B. Delmon, *Powder Technol.* **1973**, *7*, 21–38.
[46] V. Vibhu, I. C. Vinke, F. Zaravelis, S. G. Neophytides, D. K. Niakolas, R.-A. Eichel, L. G. J. de Haart, *Energies* **2022**, *15*, 2726.
[47] M. Kusnezoff, N. Trofimenko, M. Müller, A. Michaelis, *Materials (Basel)* **2016**, *9*, 906.
[48] S. E. Wolf, V. Vibhu, E. Tröster, I. C. Vinke, R.-A. Eichel, L. G. J. de Haart, *Electrolysis Cells, Energies* **2022**, *15*, 5449.
[49] V. Baecker, *Montpellier RIO Imaging* **2010**, 1–93.
[50] C. Ni, M. Cassidy, J. T. S. Irvine, *J. Eur. Ceram. Soc.* **2018**, *38*, 5463–5470.
[51] S. D. Ebbesen, X. Sun, M. B. Mogensen, *Faraday Discuss.* **2015**, *182*, 393–422.
[52] J. V. Kildgaard, H. A. Hansen, T. Vegge, *Materials Today Advances* **2020**, *8*, 100111.
[53] F. Kundracik, M. Hartmanová, J. Müllerová, M. Jergel, I. Kostič, R. Tucoulou, *Mater. Sci. Eng. B* **2001**, *84*, 167–175.
[54] E. Ioannidou, *J. Catal.* **2021**, *404*, 174–186.
[55] X. G. Cao, S. P. Jiang, *Int. J. Hydrogen Energy* **2016**, *41*, 1203–1212.
[56] D. Papurello, D. Menichini, A. Lanzini, *Electrochim. Acta* **2017**, *258*, 98–109.
[57] P. Caliandro, A. Nakajo, S. Diethelm, J. Van Herle, *J. Power Sources* **2019**, *436*, 226838.
[58] D. A. Osinkin, N. M. Bogdanovich, A. L. Gavrilyuk, *Electrochim. Acta* **2016**, *199*, 108–115.
[59] A. Leonide, Y. Apel, E. Ivers-Tiffee, *ECS Trans.* **2009**, *198*, 1–109.
[60] C. Grosselindemann, N. Russner, S. Dierickx, F. Wankmüller, A. Weber, *J. Electrochem. Soc.* **2021**, *168*, 124506.
[61] N. S. C. Priya, K. Sandhya, D. N. Rajendran, *Electrochemical Energy Technology* **2018**, *3*, 49–53.
[62] S. Primdahl, Y. L. Liu, *J. Electrochem. Soc.* **2002**, *149*, A1466.
[63] M. Riegraf, R. Costa, G. Schiller, K. A. Friedrich, S. Dierickx, A. Weber, *J. Electrochem. Soc.* **2019**, *166*, F865–F872.
[64] P. S. Manning, J. D. Sirman, J. A. Kilner, *Solid State Ionics* **1996**, *93*, 125–132.
[65] Y. Chen, Y. Bu, Y. Zhang, R. Yan, D. Ding, B. Zhao, S. Yoo, D. Dang, R. Hu, C. Yang, M. Liu, A. Highly Efficient, *Adv. Energy Mater.* **2017**, *7*, 1601890.
[66] A. Leonide, *SOFC modelling and parameter identification by means of impedance spectroscopy* **2010**, PhD thesis.
[67] T. L. Skafte, Z. Guan, M. L. Machala, C. B. Gopal, M. Monti, L. Martinez, E. Stamate, S. Sanna, J. A. Garrido Torres, E. J. Crumlin, M. García-Melchor, M. Bajdich, W. C. Chueh, C. Graves, *Nat. Energy* **2019**, *4*, 846–855.
[68] Q. Li, G. Li, *Ionics* **2021**, *27*, 3063–3076.
[69] H. Wendt, G. Kreysa, *Electrochemical engineering: science and technology in chemical and other industries* Springer Science & Business Media **1999**.
[70] M. Riegraf, V. Yurkiv, R. Costa, G. Schiller, K. A. Friedrich, *ChemSusChem.* **2017**, *10*, 587–599.
[71] W. Lin, W. Su, Y. Li, T.-W. Chiu, M. Singh, Z. Pan, L. Fan, *Small* **2023**, *19*, 2303305.
[72] Y. Li, Y. Li, S. Zhang, C. Ren, Y. Jing, F. Cheng, Q. Wu, P. Lund, L. Fan, *ACS Appl. Mater. Interfaces* **2022**, *14*, 9138–9150.
[73] J. Uecker, I. D. Unachukwu, V. Vibhu, I. C. Vinke, R.-A. Eichel, L. G. J. de Haart, *Electrochim. Acta* **2023**, *452*, 142320.
[74] L. Holzer, B. Iwanschitz, T. Hocker, B. Münch, M. Prestat, D. Wiedenmann, U. Vogt, P. Holtappels, J. Sfeir, A. Mai, T. Graule, *J. Power Sources* **2011**, *196*, 1279–1294.
[75] J. Kubota, S. Hashimoto, T. Shindo, K. Yashiro, T. Matsui, K. Yamaji, H. Kishimoto, T. Kawada, *Fuel Cells* **2017**, *17*, 402–406.
[76] F. Monaco, D. Ferreira-Sanchez, M. Hubert, B. Morel, D. Montinaro, D. Grolimund, J. Laurencin, *Int. J. Hydrogen Energy* **2021**, *46*, 31533–31549.
[77] V. Vibhu, S. Yildiz, I. C. Vinke, R. A. Eichel, J. M. Bassat, L. G. J. de Haart, *J. Electrochem. Soc.* **2019**, *166*, F102–F108.

Manuscript received: October 31, 2023
Revised manuscript received: January 15, 2024
Version of record online: February 21, 2024